

Hitomi X-ray observation of the pulsar wind nebula G21.5–0.9

Hitomi Collaboration, Felix AHARONIAN,^{1,2,3} Hiroki AKAMATSU,⁴
Fumie AKIMOTO,⁵ Steven W. ALLEN,^{6,7,8} Lorella ANGELINI,⁹ Marc AUDARD,¹⁰
Hisamitsu AWAKI,¹¹ Magnus AXELSSON,¹² Aya BAMBA,^{13,14}
Marshall W. BAUTZ,¹⁵ Roger BLANDFORD,^{6,7,8} Laura W. BRENNEMAN,¹⁶
Gregory V. BROWN,¹⁷ Esra BULBUL,¹⁵ Edward M. CACKETT,¹⁸
Maria CHERNYAKOVA,¹ Meng P. CHIAO,⁹ Paolo S. COPPI,^{19,20} Elisa COSTANTINI,⁴
Jelle DE PLAA,⁴ Cor P. DE VRIES,⁴ Jan-Willem DEN HERDER,⁴ Chris DONE,²¹
Tadayasu DOTANI,²² Ken EBISAWA,²² Megan E. ECKART,⁹ Teruaki ENOTO,^{23,24}
Yuichiro EZOE,²⁵ Andrew C. FABIAN,²⁶ Carlo FERRIGNO,¹⁰ Adam R. FOSTER,¹⁶
Ryuichi FUJIMOTO,²⁷ Yasushi FUKAZAWA,²⁸ Akihiro FURUZAWA,²⁹
Massimiliano GALEAZZI,³⁰ Luigi C. GALLO,³¹ Poshak GANDHI,³²
Margherita GIUSTINI,⁴ Andrea GOLDWURM,^{33,34} Liyi GU,⁴ Matteo GUAINAZZI,³⁵
Yoshito HABA,³⁶ Kouichi HAGINO,³⁷ Kenji HAMAGUCHI,^{9,38} Ilana M. HARRUS,^{9,38}
Isamu HATSUKADE,³⁹ Katsuhiko HAYASHI,^{22,40} Takayuki HAYASHI,⁴⁰
Kiyoshi HAYASHIDA,⁴¹ Junko S. HIRAGA,⁴² Ann HORNSCHMEIER,⁹
Akio HOSHINO,⁴³ John P. HUGHES,⁴⁴ Yuto ICHINOHE,²⁵ Ryo IZUKA,²²
Hajime INOUE,⁴⁵ Yoshiyuki INOUE,²² Manabu ISHIDA,²² Kumi ISHIKAWA,²²
Yoshitaka ISHISAKI,²⁵ Masachika IWAI,²² Jelle KAASTRA,^{4,46} Tim KALLMAN,⁹
Tsuneyoshi KAMAE,¹³ Jun KATAOKA,⁴⁷ Satoru KATSUDA,⁴⁸ Nobuyuki KAWAI,⁴⁹
Richard L. KELLEY,⁹ Caroline A. KILBOURNE,⁹ Takao KITAGUCHI,²⁸
Shunji KITAMOTO,⁴³ Tetsu KITAYAMA,⁵⁰ Takayoshi KOHMURA,³⁷
Motohide KOKUBUN,²² Katsuji KOYAMA,⁵¹ Shu KOYAMA,²²
Peter KRETSCHMAR,⁵² Hans A. KRIMM,^{53,54} Aya KUBOTA,⁵⁵ Hideyo KUNIEDA,⁴⁰
Philippe LAURENT,^{33,34} Shiu-Hang LEE,²³ Maurice A. LEUTENEGGER,^{9,38}
Olivier LIMOUSIN,³⁴ Michael LOEWENSTEIN,^{9,56} Knox S. LONG,⁵⁷ David LUMB,³⁵
Greg MADEJSKI,⁶ Yoshitomo MAEDA,²² Daniel MAIER,^{33,34} Kazuo MAKISHIMA,⁵⁸
Maxim MARKEVITCH,⁹ Hironori MATSUMOTO,⁴¹ Kyoko MATSUSHITA,⁵⁹
Dan MCCAMMON,⁶⁰ Brian R. McNAMARA,⁶¹ Missagh MEHDIPOUR,⁴
Eric D. MILLER,¹⁵ Jon M. MILLER,⁶² Shin MINESHIGE,²³ Kazuhisa MITSUDA,²²
Ikuyuki MITSUISHI,⁴⁰ Takuya MIYAZAWA,⁶³ Tsunefumi MIZUNO,^{28,64}
Hideyuki MORI,⁹ Koji MORI,³⁹ Koji MUKAI,^{9,38} Hiroshi MURAKAMI,⁶⁵
Richard F. MUSHOTZKY,⁵⁶ Takao NAKAGAWA,²² Hiroshi NAKAJIMA,⁴¹
Takeshi NAKAMORI,⁶⁶ Shinya NAKASHIMA,⁵⁸ Kazuhiro NAKAZAWA,^{13,14}
Kumiko K. NOBUKAWA,⁶⁷ Masayoshi NOBUKAWA,⁶⁸ Hirofumi NODA,^{69,70}

Hirokazu ODAKA,⁶ Takaya OHASHI,²⁵ Masanori OHNO,²⁸ Takashi OKAJIMA,⁹
 Naomi OTA,⁶⁷ Masanobu OZAKI,²² Frits PAERELS,⁷¹ Stéphane PALTANI,¹⁰
 Robert PETRE,⁹ Ciro PINTO,²⁶ Frederick S. PORTER,⁹ Katja POTTSCHMIDT,^{9,38}
 Christopher S. REYNOLDS,⁵⁶ Samar SAFI-HARB,⁷² Shinya SAITO,⁴³
 Kazuhiro SAKAI,⁹ Toru SASAKI,⁵⁹ Goro SATO,²² Kosuke SATO,⁵⁹ Rie SATO,²²
 Makoto SAWADA,⁷³ Norbert SCHARTEL,⁵² Peter J. SERLEMTSOS,⁹
 Hiromi SETA,²⁵ Megumi SHIDATSU,⁵⁸ Aurora SIMIONESCU,²²
 Randall K. SMITH,¹⁶ Yang SOONG,⁹ Łukasz STAWARZ,⁷⁴ Yasuharu SUGAWARA,²²
 Satoshi SUGITA,⁴⁹ Andrew SZYMKOWIAK,²⁰ Hiroyasu TAJIMA,⁵
 Hiromitsu TAKAHASHI,²⁸ Tadayuki TAKAHASHI,²² Shin'ichiro TAKEDA,⁶³
 Yoh TAKEI,²² Toru TAMAGAWA,⁷⁵ Takayuki TAMURA,²² Takaaki TANAKA,⁵¹
 Yasuo TANAKA,^{76,22} Yasuyuki T. TANAKA,²⁸ Makoto S. TASHIRO,⁷⁷
 Yuzuru TAWARA,⁴⁰ Yukikatsu TERADA,⁷⁷ Yuichi TERASHIMA,¹¹
 Francesco TOMBESI,^{9,38,78} Hiroshi TOMIDA,²² Yohko TSUBOI,⁴⁸
 Masahiro TSUJIMOTO,²² Hiroshi TSUNEMI,⁴¹ Takeshi Go TSURU,⁵¹
 Hiroyuki UCHIDA,^{51,*} Hideki UCHIYAMA,⁷⁹ Yasunobu UCHIYAMA,⁴³
 Shutaro UEDA,²² Yoshihiro UEDA,²³ Shin'ichiro UNO,⁸⁰ C. Megan URRY,²⁰
 Eugenio URSINO,³⁰ Shin WATANABE,²² Norbert WERNER,^{81,82,28}
 Dan R. WILKINS,⁶ Brian J. WILLIAMS,⁵⁷ Shinya YAMADA,²⁵
 Hiroya YAMAGUCHI,^{9,56} Kazutaka YAMAOKA,^{5,40} Noriko Y. YAMASAKI,²²
 Makoto YAMAUCHI,³⁹ Shigeo YAMAUCHI,⁶⁷ Tahir YAQOUB,^{9,38} Yoichi YATSU,⁴⁹
 Daisuke YONETOKU,²⁷ Irina ZHURAVLEVA,^{6,7} Abderahmen ZOGHBI,⁶²
 Toshiki SATO,^{25,22} Nozomu NAKANIWA,²² Hiroaki MURAKAMI,^{13,14}
 and Benson GUEST⁷²

¹Dublin Institute for Advanced Studies, 31 Fitzwilliam Place, Dublin 2, Ireland

²Max-Planck-Institut für Kernphysik, P.O. Box 103980, 69029 Heidelberg, Germany

³Gran Sasso Science Institute, viale Francesco Crispi, 7 67100 L'Aquila (AQ), Italy

⁴SRON Netherlands Institute for Space Research, Sorbonnelaan 2, 3584 CA Utrecht, The Netherlands

⁵Institute for Space-Earth Environmental Research, Nagoya University, Furo-cho, Chikusa-ku, Nagoya, Aichi 464-8601, Japan

⁶Kavli Institute for Particle Astrophysics and Cosmology, Stanford University, 452 Lomita Mall, Stanford, CA 94305, USA

⁷Department of Physics, Stanford University, 382 Via Pueblo Mall, Stanford, CA 94305, USA

⁸SLAC National Accelerator Laboratory, 2575 Sand Hill Road, Menlo Park, CA 94025, USA

⁹NASA, Goddard Space Flight Center, 8800 Greenbelt Road, Greenbelt, MD 20771, USA

¹⁰Department of Astronomy, University of Geneva, ch. d'Écogia 16, CH-1290 Versoix, Switzerland

¹¹Department of Physics, Ehime University, 2-5 Bunkyo-cho, Matsuyama, Ehime 790-8577, Japan

¹²Department of Physics and Oskar Klein Center, Stockholm University, 106 91 Stockholm, Sweden

¹³Department of Physics, The University of Tokyo, 7-3-1 Hongo, Bunkyo-ku, Tokyo 113-0033, Japan

¹⁴Research Center for the Early Universe, School of Science, The University of Tokyo, 7-3-1 Hongo, Bunkyo-ku, Tokyo 113-0033, Japan

¹⁵Kavli Institute for Astrophysics and Space Research, Massachusetts Institute of Technology, 77 Massachusetts Avenue, Cambridge, MA 02139, USA

¹⁶Smithsonian Astrophysical Observatory, 60 Garden St., MS-4. Cambridge, MA 02138, USA

¹⁷Lawrence Livermore National Laboratory, 7000 East Avenue, Livermore, CA 94550, USA

¹⁸Department of Physics and Astronomy, Wayne State University, 666 W. Hancock St, Detroit, MI 48201, USA

- ¹⁹Department of Astronomy, Yale University, New Haven, CT 06520-8101, USA
- ²⁰Department of Physics, Yale University, New Haven, CT 06520-8120, USA
- ²¹Centre for Extragalactic Astronomy, Department of Physics, University of Durham, South Road, Durham, DH1 3LE, UK
- ²²Japan Aerospace Exploration Agency, Institute of Space and Astronautical Science, 3-1-1 Yoshino-dai, Chuo-ku, Sagami-hara, Kanagawa 252-5210, Japan
- ²³Department of Astronomy, Kyoto University, Kitashirakawa-Oiwake-cho, Sakyo-ku, Kyoto, Kyoto 606-8502, Japan
- ²⁴The Hakubi Center for Advanced Research, Kyoto University, Yoshida-Ushinomiya-cho, Sakyo-ku, Kyoto, Kyoto 606-8302, Japan
- ²⁵Department of Physics, Tokyo Metropolitan University, 1-1 Minami-Osawa, Hachioji, Tokyo 192-0397, Japan
- ²⁶Institute of Astronomy, University of Cambridge, Madingley Road, Cambridge, CB3 0HA, UK
- ²⁷Faculty of Mathematics and Physics, Kanazawa University, Kakuma-machi, Kanazawa, Ishikawa 920-1192, Japan
- ²⁸School of Science, Hiroshima University, 1-3-1 Kagamiyama, Higashi-Hiroshima, Hiroshima 739-8526, Japan
- ²⁹Fujita Health University, 1-98 Dengakugakubo, Kutsukake-cho, Toyoake, Aichi 470-1192, Japan
- ³⁰Physics Department, University of Miami, 1320 Campo Sano Dr., Coral Gables, FL 33146, USA
- ³¹Department of Astronomy and Physics, Saint Mary's University, 923 Robie Street, Halifax, NS, B3H 3C3, Canada
- ³²Department of Physics and Astronomy, University of Southampton, Highfield, Southampton, SO17 1BJ, UK
- ³³Laboratoire APC, 10 rue Alice Domon et Léonie Duquet, 75013 Paris, France
- ³⁴CEA Saclay, 91191 Gif sur Yvette, France
- ³⁵European Space Research and Technology Center, Keplerlaan 1 2201 AZ Noordwijk, The Netherlands
- ³⁶Department of Physics and Astronomy, Aichi University of Education, 1 Hirosawa, Igaya-cho, Kariya, Aichi 448-8543, Japan
- ³⁷Department of Physics, Tokyo University of Science, 2641 Yamazaki, Noda, Chiba 278-8510, Japan
- ³⁸Department of Physics, University of Maryland Baltimore County, 1000 Hilltop Circle, Baltimore, MD 21250, USA
- ³⁹Department of Applied Physics and Electronic Engineering, University of Miyazaki, 1-1 Gakuen Kibanadai-Nishi, Miyazaki, Miyazaki 889-2192, Japan
- ⁴⁰Department of Physics, Nagoya University, Furo-cho, Chikusa-ku, Nagoya, Aichi 464-8602, Japan
- ⁴¹Department of Earth and Space Science, Osaka University, 1-1 Machikaneyama-cho, Toyonaka, Osaka 560-0043, Japan
- ⁴²Department of Physics, Kwansei Gakuin University, 2-1 Gakuen, Sanda, Hyogo 669-1337, Japan
- ⁴³Department of Physics, Rikkyo University, 3-34-1 Nishi-Ikebukuro, Toshima-ku, Tokyo 171-8501, Japan
- ⁴⁴Department of Physics and Astronomy, Rutgers University, 136 Frelinghuysen Road, Piscataway, NJ 08854, USA
- ⁴⁵Meisei University, 2-1-1 Hodokubo, Hino, Tokyo 191-8506, Japan
- ⁴⁶Leiden Observatory, Leiden University, PO Box 9513, 2300 RA Leiden, The Netherlands
- ⁴⁷Research Institute for Science and Engineering, Waseda University, 3-4-1 Ohkubo, Shinjuku, Tokyo 169-8555, Japan
- ⁴⁸Department of Physics, Chuo University, 1-13-27 Kasuga, Bunkyo, Tokyo 112-8551, Japan
- ⁴⁹Department of Physics, Tokyo Institute of Technology, 2-12-1 Ookayama, Meguro-ku, Tokyo 152-8550, Japan
- ⁵⁰Department of Physics, Toho University, 2-2-1 Miyama, Funabashi, Chiba 274-8510, Japan
- ⁵¹Department of Physics, Kyoto University, Kitashirakawa-Oiwake-cho, Sakyo, Kyoto, Kyoto 606-8502, Japan

- ⁵²European Space Astronomy Center, Camino Bajo del Castillo, s/n., 28692 Villanueva de la Cañada, Madrid, Spain
- ⁵³Universities Space Research Association, 7178 Columbia Gateway Drive, Columbia, MD 21046, USA
- ⁵⁴National Science Foundation, 4201 Wilson Blvd, Arlington, VA 22230, USA
- ⁵⁵Department of Electronic Information Systems, Shibaura Institute of Technology, 307 Fukasaku, Minuma-ku, Saitama, Saitama 337-8570, Japan
- ⁵⁶Department of Astronomy, University of Maryland, College Park, MD 20742, USA
- ⁵⁷Space Telescope Science Institute, 3700 San Martin Drive, Baltimore, MD 21218, USA
- ⁵⁸Institute of Physical and Chemical Research, 2-1 Hirosawa, Wako, Saitama 351-0198, Japan
- ⁵⁹Department of Physics, Tokyo University of Science, 1-3 Kagurazaka, Shinjuku-ku, Tokyo 162-8601, Japan
- ⁶⁰Department of Physics, University of Wisconsin, Madison, WI 53706, USA
- ⁶¹Department of Physics and Astronomy, University of Waterloo, 200 University Avenue West, Waterloo, Ontario, N2L 3G1, Canada
- ⁶²Department of Astronomy, University of Michigan, 1085 South University Avenue, Ann Arbor, MI 48109, USA
- ⁶³Okinawa Institute of Science and Technology Graduate University, 1919-1 Tancha, Onna-son, Kunigami-gun, Okinawa 904-0495, Japan
- ⁶⁴Hiroshima Astrophysical Science Center, Hiroshima University, 1-3-1 Kagamiyama, Higashi-Hiroshima, Hiroshima 739-8526, Japan
- ⁶⁵Faculty of Liberal Arts, Tohoku Gakuin University, 2-1-1 Tenjinzawa, Izumi-ku, Sendai, Miyagi 981-3193, Japan
- ⁶⁶Faculty of Science, Yamagata University, 1-4-12 Kojirakawa-machi, Yamagata, Yamagata 990-8560, Japan
- ⁶⁷Department of Physics, Nara Women's University, Kitauoyanishi-machi, Nara, Nara 630-8506, Japan
- ⁶⁸Department of Teacher Training and School Education, Nara University of Education, Takabatake-cho, Nara, Nara 630-8528, Japan
- ⁶⁹Frontier Research Institute for Interdisciplinary Sciences, Tohoku University, 6-3 Aramaki-zaaoba, Aoba-ku, Sendai, Miyagi 980-8578, Japan
- ⁷⁰Astronomical Institute, Tohoku University, 6-3 Aramaki-zaaoba, Aoba-ku, Sendai, Miyagi 980-8578, Japan
- ⁷¹Astrophysics Laboratory, Columbia University, 550 West 120th Street, New York, NY 10027, USA
- ⁷²Department of Physics and Astronomy, University of Manitoba, Winnipeg, MB R3T 2N2, Canada
- ⁷³Department of Physics and Mathematics, Aoyama Gakuin University, 5-10-1 Fuchinobe, Chuo-ku, Sagami-hara, Kanagawa 252-5258, Japan
- ⁷⁴Astronomical Observatory of Jagiellonian University, ul. Orla 171, 30-244 Kraków, Poland
- ⁷⁵RIKEN Nishina Center, 2-1 Hirosawa, Wako, Saitama 351-0198, Japan
- ⁷⁶Max-Planck-Institut für extraterrestrische Physik, Giessenbachstrasse 1, 85748 Garching, Germany
- ⁷⁷Department of Physics, Saitama University, 255 Shimo-Okubo, Sakura-ku, Saitama, Saitama 338-8570, Japan
- ⁷⁸Department of Physics, University of Rome "Tor Vergata", Via della Ricerca Scientifica 1, I-00133 Rome, Italy
- ⁷⁹Faculty of Education, Shizuoka University, 836 Ohya, Suruga-ku, Shizuoka, Shizuoka 422-8529, Japan
- ⁸⁰Faculty of Health Sciences, Nihon Fukushi University, 26-2 Higashi Haemi-cho, Handa, Aichi 475-0012, Japan
- ⁸¹MTA-Eötvös University Lendület Hot Universe Research Group, Pázmány Péter sétány 1/A, Budapest, 1117, Hungary
- ⁸²Department of Theoretical Physics and Astrophysics, Faculty of Science, Masaryk University, Kotlářská 2, Brno, 602 00, Czech Republic

*E-mail: uchida@cr.scphys.kyoto-u.ac.jp

Received 2017 December 13; Accepted 2018 February 14

Abstract

We present results from the Hitomi X-ray observation of a young composite-type supernova remnant (SNR) G21.5–0.9, whose emission is dominated by the pulsar wind nebula (PWN) contribution. The X-ray spectra in the 0.8–80 keV range obtained with the Soft X-ray Spectrometer (SXS), Soft X-ray Imager, and Hard X-ray Imager (HXI) show a significant break in the continuum as previously found with the NuSTAR observation. After taking into account all known emissions from the SNR other than the PWN itself, we find that the Hitomi spectra can be fitted with a broken power law with photon indices of $\Gamma_1 = 1.74 \pm 0.02$ and $\Gamma_2 = 2.14 \pm 0.01$ below and above the break at 7.1 ± 0.3 keV, which is significantly lower than the NuSTAR result (~ 9.0 keV). The spectral break cannot be reproduced by time-dependent particle injection one-zone spectral energy distribution models, which strongly indicates that a more complex emission model is needed, as suggested by recent theoretical models. We also search for narrow emission or absorption lines with the SXS, and perform a timing analysis of PSR J1833–1034 with the HXI and the Soft Gamma-ray Detector. No significant pulsation is found from the pulsar. However, unexpectedly, narrow absorption line features are detected in the SXS data at 4.2345 keV and 9.296 keV with a significance of 3.65σ . While the origin of these features is not understood, their mere detection opens up a new field of research and was only possible with the high resolution, sensitivity, and ability to measure extended sources provided by an X-ray microcalorimeter.

Key words: ISM: individual objects (G21.5–0.9) — ISM: supernova remnants — pulsars: individual (PSR J1833–1034)

1 Introduction

A pulsar wind nebula (PWN) is driven by relativistic particles and the magnetic field generated by its central compact object, a pulsar inside a supernova remnant (SNR) shell (Pacini & Salvati 1973; Rees & Gunn 1974; Kennel & Coroniti 1984). A bubble is formed beyond a termination shock where the relativistic wind of non-thermal electrons and positrons interact with the surrounding ejecta (e.g., Fang & Zhang 2010). The resultant emission is dominated by centrally peaked synchrotron radiation from radio to X-rays and inverse Compton scattering (IC) at higher energies. The observed spectra of PWNe are basically characterized by a power law with a hard spectral index $\alpha \sim -0.3$ –0 at radio wavelengths and a steeper photon index in X-rays, $\Gamma \equiv 1 - \alpha \sim 2$ (cf. Gaensler & Slane 2006). Because the break energy is associated with the acceleration process and the aging of the particles, a wide-band analysis helps us understand the evolution of PWNe (Reynolds & Chevalier 1984), although the nature of the spectral steepening is still under debate.

One of the best observed examples of a young PWN is G21.5–0.9 (Altenhoff et al. 1970; Becker & Szymkowiak 1981), which substitutes for the Crab nebula (Kirsch

et al. 2005) as a standard candle or a calibration target for X-ray satellites. Several X-ray studies of this nebula with Chandra and XMM-Newton show a non-thermal power-law spectrum with no line emission (Slane et al. 2000; Safi-Harb et al. 2001; Warwick et al. 2001). Using G21.5–0.9, Tsujimoto et al. (2011) performed a comprehensive cross calibration of Chandra, INTEGRAL, RXTE, Suzaku, Swift, and XMM-Newton as one of the activities of the International Astronomical Consortium for High Energy Calibration (IACHEC). They separated these instruments into two groups: Chandra ACIS, Suzaku XIS, Swift XRT, and XMM-Newton EPIC (MOS and pn) for the soft band (<10 keV); INTEGRAL IBIS-ISGRI, RXTE PCA, and Suzaku HXD-PIN for the hard band (>10 keV). One of their results of interest to scientific studies is a significant difference in the photon indices $\Gamma \sim 1.84$ and ~ 2.05 taken from the joint fittings of the soft- and hard-band instruments, respectively. This study implies spectral steepening of G21.5–0.9 in the X-ray band, as indicated by the preceding soft-band analyses (e.g., Matheson & Safi-Harb 2010, in addition to the above), although the radially dependent Γ should be considered in the discussion of the nature of the steepening. Nynka et al. (2014) observed G21.5–0.9 with NuSTAR and revealed a high-energy spectral feature in the band of 3–45 keV. The spectrum is represented by a broken power law with a break energy of ~ 9 keV. A broadband spectral energy distribution (SED) model built

[†] The corresponding authors are Hiroyuki Uchida, Takaaki Tanaka, Samar Safi-Harb, Masahiro Tsujimoto, Yukikatsu Terada, Aya Bamba, Yoshitomo Maeda, and John P. Hughes.

by Tanaka and Takahara (2011) gives a poor fit to the NuSTAR spectrum and thus Nynka et al. (2014) suggested that further modeling is required to explain the wide-band spectrum of G21.5–0.9. They proposed some extra aspects to take into account, for example more complex electron injection spectra, additional loss processes (e.g., diffusion), or radial dependence of the PWN parameters.

One of the clear differences between G21.5–0.9 and the Crab is the existence of faint thin-thermal extended emission (Bocchino et al. 2005; Matheson & Safi-Harb 2005, 2010). This fact illustrates how accumulated calibration observations help to reveal a shell component in a Crab-like PWN. However, given the brightness of the PWN and the relatively weak thermal X-ray emission from G21.5–0.9, the parameters of the thermal emission from the shell are still poorly determined. In particular, we have no information on Fe-K emission line, which is common in young SNRs such as Cassiopeia A (Hughes et al. 2000). Depending on the magnetic field strength of the powering pulsar, the emission from the pulsar itself also reveals line features in the X-ray band due to the cyclotron effect (Meszaros & Nagel 1985). It is thus of interest to search for emission/absorption line structures with excellent energy resolution detectors.

PSR J1833–1034 was discovered at the center of G21.5–0.9 in the radio band (Gupta et al. 2005; Camilo et al. 2006) and GeV gamma-ray band (Abdo et al. 2013). The characteristic age of the pulsar is estimated to be 4850 yr from the period of ~ 61.9 ms and the period derivative of $\sim 2.0 \times 10^{-13} \text{ s s}^{-1}$, however the dynamics of its associated PWN indicates a much younger age of 870^{+200}_{-150} yr (Bietenholz & Bartel 2008), which makes this pulsar one of the youngest and the most energetic systems in our Galaxy. On the other hand, no significant pulsation has been found yet in the X-ray band (Bocchino et al. 2005; Camilo et al. 2006; Matheson & Safi-Harb 2010), although the central pulsar is very energetic (Kargaltsev & Pavlov 2008; Bamba et al. 2010). This is likely due to the contamination from the very bright PWN. Typically, X-ray emission from a pulsar is harder than that from a PWN (Kargaltsev & Pavlov 2008), and therefore the hard X-ray band is suitable to search for the coherent pulsation. The Hitomi Hard X-ray Imager (HXI) has good sensitivity, low background (Matsumoto et al. 2017; Nakazawa et al. 2018; Hagino et al. 2018), and good timing accuracy (Terada et al. 2017) with the rather long time duration of the G21.5–0.9 observation of 329 ks, and thus it could have higher sensitivity for the search for the coherent pulsation from the pulsar.

In this paper we report on observational results of G21.5–0.9 with Hitomi (formerly known as ASTRO-H; Takahashi et al. 2016). The observation was performed

during the commissioning and performance verification phase. We obtained simultaneous data of all the instruments aboard with the longest exposure among the targeted celestial sources Hitomi observed. Here we focus on the following three studies: wide-band spectroscopy, narrow emission or absorption line searches, and a timing analysis. In section 2, we present detailed information on the Hitomi observation and the data reduction. In section 3, we perform the joint fitting of the G21.5–0.9 data and discuss the result. The blind search for emission or absorption lines and the timing analysis are presented in sections 4 and 5, respectively. All the results are summarized in section 6.

2 Observation and data reduction

G21.5–0.9 was observed with Hitomi on 2016 March 19–23 during the instrument commissioning phase of the satellite. We analyzed data from the four instruments aboard Hitomi: the Soft X-ray Spectrometer (SXS; Kelley et al. 2016), the Soft X-ray Imager (SXI; Tanaka et al. 2018), the Hard X-ray Imager (HXI; Nakazawa et al. 2018), and the Soft Gamma-ray Detector (SGD; Watanabe et al. 2016). The Soft X-ray Telescope (SXT; Soong et al. 2014; Okajima et al. 2016) consists of two modules of X-ray mirrors, SXT-S and SXT-I, which focus X-rays for the SXS and SXI, respectively. The HXI system consists of two sets of detector modules referred to as HXI1 and HXI2. Two sets of the Hard X-ray Telescope (HXT; Awaki et al. 2014) are used to focus hard-band X-rays for each of the HXI sensors. The SGD system consists of two sets of detector modules referred to as SGD1 and SGD2. Detailed information on the observation is summarized in table 1.

We combined all the data of four different sequence IDs (see table 1) for our spectral analysis. We performed the data reduction with version 6.20 of the HEASoft tools, which is compatible with version 005b of the Hitomi Software released on 2017 March 6. We applied the Hitomi Calibration Database version 6 released on 2017 March 6 for the following analysis. Note that the gate valve of the SXS remained closed during the observation, which significantly reduced the effective area of the SXS below 2 keV. We applied the “Crab ratio correction factor” for modeling the effective area of SXS (Tsujimoto et al. 2018). In the SXI data analysis, we carefully excluded events detected in “minus-Z day earth (MZDYE)” intervals, during which the SXI has many pixels affected by light leakage from the day earth (Nakajima et al. 2018). We eliminated the SGD data for the wide-band spectroscopy since the observation was performed during the turn-on phase of SGD1 and we have no SGD2 data.

In figure 1, we present the full-band images of G21.5–0.9 taken by the SXS, SXI, and HXI. We note that

Table 1. Observation log.

Target	Obs. Date	(RA, Dec) _{J2000.0}	Sequence ID	Effective Exposure (ks)
G21.5–0.9	2016 March 19–23	(278.39, –10.57)	100050010–100050040	165 (SXS) / 51 (SXI) / 99 (HXI) / 255 (SGD)

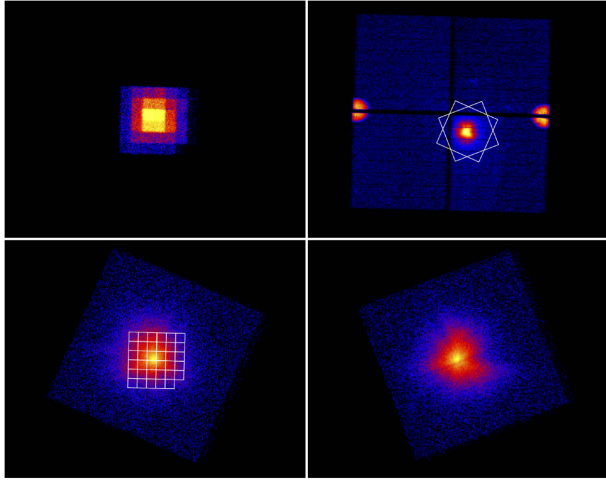


Fig. 1. Top left: SXS sky coordinate image of G21.5–0.9. Top right: SXI image of the source and the surrounding region. Two calibration-source regions are also included in the image. The FOV of the HXI is indicated by the solid squares. Bottom: HXI1 (left) and HXI2 (right) images of G21.5–0.9. The SXS pixel array (white squares) overlaid on the HXI1 image. (Color online)

there are no significant transient sources in the vicinity of G21.5–0.9 within the field of view (FOV) of the SXI. As previously reported by Slane et al. (2000), G21.5–0.9 has a core of wind termination shock surrounded by a synchrotron nebula with a radius of $\sim 30''$, which is consistent with the centrally peaked profile shown in figure 1. G21.5–0.9 also has a faint $150''$ -radius halo that almost covers the $3' \times 3'$ SXS FOV.

To extract the SXS spectrum, we used all 35 pixels. The source extraction region for the SXI and HXI is a circle with a $\sim 3'$ radius centered at (RA, Dec) = ($18^{\text{h}}33^{\text{m}}33^{\text{s}}.57$, $-10^{\circ}34'07''.5$) in the equinox J2000.0, which is the position of the central pulsar, PSR J1833–1034. Spectral fittings were performed with the X-ray Spectral Fitting Package (XSPEC) version 12.9.0u (Arnaud 1996) with the Cash statistics (Cash 1979). We did not rebin the spectra since the Cash statistics can deal with low-count bins as opposed to the χ^2 fitting method. We generated redistribution matrix files for the SXS and SXI with `sxsmkrmf` and `sxirmf`, respectively. We ran `aharfgen` (Yaqoob et al. 2018) to generate ancillary response files for the SXS and SXI and response files for the HXI. Since G21.5–0.9 has a faint diffuse extended halo out to $\sim 140''$ from the pulsar (e.g., Matheson & Safi-Harb 2005), we generated the response files by inputting a Chandra image (0.5–10.0 keV) to `aharfgen` to take into account the spatial extent. Note,

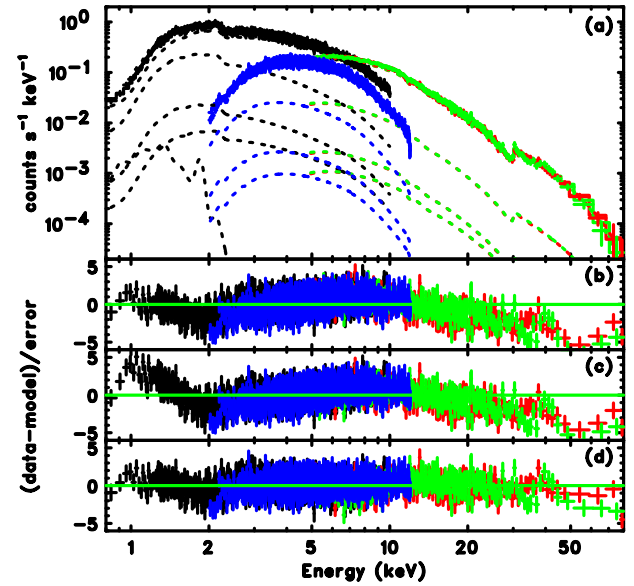


Fig. 2. Wide-band spectra of G21.5–0.9 obtained with the SXI (black; 0.8–10.0 keV), HXI1 (red; 5.0–80.0 keV), HXI2 (green; 5.0–80.0 keV), and SXS (blue; 2.0–12.0 keV). The data is rebinned only for plotting purposes. The best-fit model (composite + Broken PL; see text and table 2) is overlaid with the solid lines in panel (a). The dotted lines indicate all the additive components in the model. Panels (b), (c), and (d) show residuals from the single PL, composite + PL, and composite+Broken PL models, respectively. (Color online)

however, that whether the assumed source type is “extended” or “point-like,” our spectral analysis results are unaffected. The background spectrum for the SXI is extracted from a source-free region of the on-axis segment (CCD2CD). Off-source spectra are used for the HXI backgrounds as well.

3 Wide-band spectroscopy

3.1 Analysis

Figure 2a shows the background-subtracted spectra of G21.5–0.9 (0.8–10.0 keV for the SXI, 5.0–80.0 keV for the HXI, and 2.0–12.0 keV for the SXS). The featureless spectral shape already suggests that the emission is dominated by non-thermal X-ray emission, as reported by previous X-ray studies (Slane et al. 2000; Safi-Harb et al. 2001; Warwick et al. 2001; Bocchino et al. 2005; Matheson & Safi-Harb 2010; Tsujimoto et al. 2011; Nynka et al. 2014). In order to fit the SXS, SXI, and HXI data, we first attempted a single power law (hereafter, single PL) modified by interstellar absorption using the Tuebingen–Boulder

Table 2. Spectral fitting results of the Hitomi G21.5–0.9 data.*

Parameter	Model		
	Single PL	Composite + PL	Composite + Broken PL
N_{H} (10^{22} cm^{-2})	3.50 ± 0.03	3.64 ± 0.02	3.22 ± 0.03
Γ_1	2.03 ± 0.01	2.01 ± 0.01	1.74 ± 0.02
Γ_2	–	–	2.14 ± 0.01
E_{break} (keV)	–	–	7.1 ± 0.3
$F_{\text{X,soft}}^{\dagger}$ ($10^{-11} \text{ erg s}^{-1} \text{ cm}^{-2}$)	3.39 ± 0.04	2.88 ± 0.03	4.80 ± 0.02
$F_{\text{X,hard}}^{\ddagger}$ ($10^{-11} \text{ erg s}^{-1} \text{ cm}^{-2}$)	4.96 ± 0.04	4.92 ± 0.04	4.54 ± 0.04
C-statistics (using 23035 PHA bins)/d.o.f.	25447.06/23030	25380.67/23029	24228.18/23027

*The errors are 90% confidence level.

\dagger Intrinsic flux in the 2.0–8.0 keV range for the SXI and SXS.

\ddagger Intrinsic flux in the 15.0–50.0 keV range for the HXI.

interstellar medium (ISM) absorption (TBabs in XSPEC: Wilms et al. 2000). We find that while this model fits well the spectra up to ~ 10 keV, giving a photon index of ~ 2.0 , it overpredicts the emission in the HXI band, suggesting a spectral break. The residuals and the fitting parameters are shown in figure 2b and table 2, respectively. When fitting the HXI data alone with the column density frozen to its best-fit value from the broad-band fit, we find a steeper photon index of ~ 2.2 , confirming our conclusion above.

Guided by the most recent spatially resolved Chandra studies of this source (Matheson & Safi-Harb 2010; B. Guest & S. Safi-Harb in preparation; see also Bocchino et al. 2005 for the XMM-Newton study) showing that the spectrum steepens away from the source and has some weak thermal X-ray emission from the northern knot, we used a “composite” model that accounts for the emission from all but the power-law emission from the PWN (as observed with Chandra: B. Guest & S. Safi-Harb in preparation). We define the model “composite + PL” as multiple components from the pulsar, the extended halo, and the limb, a weak, thermal soft ($kT_e \sim 0.15$ keV) component from the northern knot, represented by a non-equilibrium ionization model (vpshock in XSPEC: Borkowski et al. 2001), plus a power-law component from the PWN (the most dominant component). We note here that the SXS is not sensitive to the localized thermal component due to the limited sensitivity below ~ 2 keV and the lack of spatial resolution to extract the thermal knots. We also note that the blackbody thermal component from the pulsar, PSR J1833–1034, reported by Matheson and Safi-Harb (2010) is not significant and contributes with a negligible fraction to the spectrum of the SNR obtained with Hitomi. As shown in figure 2c, we find that the model (composite + PL) is sufficient to explain the SXS data. The model, however, underpredicts or overpredicts the soft and hard X-ray emissions detected with the SXI and HXI, respectively. The result again clearly shows

negative residuals at > 10 keV, which suggests that a steeper power-law slope is required by the HXI data, as claimed by recent studies obtained in the hard X-ray band (Tsujiimoto et al. 2011; Nynka et al. 2014). The best-fit results for the composite + PL model are displayed in table 2.

We subsequently replaced the power-law model component representing the PWN with a broken power-law model (composite + Broken PL) to reproduce the spectral break. The result and residuals are presented in figures 2a and 2d, respectively. The model (composite + Broken PL) reduces the large residuals at > 10 keV seen in figure 2c. As shown in table 2, this model fits the spectra with photon indices of $\Gamma_1 = 1.74 \pm 0.02$ for the soft band and $\Gamma_2 = 2.14 \pm 0.02$ for the hard band, giving a break energy $E_{\text{break}} = 7.1 \pm 0.3$ keV. We note that the best-fit column density of $N_{\mathrm{H}} = (3.2 \pm 0.03) \times 10^{22} \text{ cm}^{-2}$ is lower than those obtained by Matheson and Safi-Harb (2010) and previous Chandra and XMM-Newton studies. This is mainly due to the difference of the abundance tables used in the spectral fittings. We use here the updated abundance table (Wilms et al. 2000), whereas most previous X-ray studies used the abundances given by Anders and Grevesse (1989). The choice, however, does not affect the other spectral parameters such as the photon indices or the break energy.

3.2 Origin of spectral break at ~ 7 keV

We know from previous Chandra X-ray studies that the spectral index for G21.5–0.9 steepens away gradually from the PSR J1833–1034 as we go out to the limb of the SNR (Matheson & Safi-Harb 2005). Here we demonstrate that the spectral softening or break required for fitting the HXI spectrum of the SNR cannot be due to this spatially varying photon index; that is, the addition of the different power-law components does not reproduce the spectrum observed

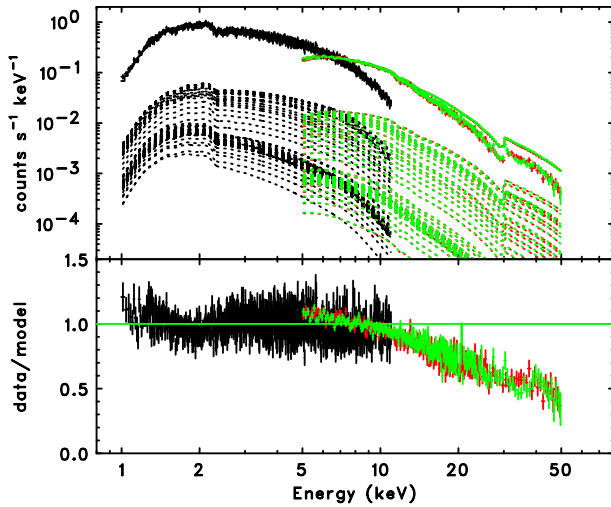


Fig. 3. The SXI (black) and HX11/2 data (red and green) fitted with the composite + PL model accounting for the spatially resolved spectroscopic study of the SNR with Chandra (B. Guest & S. Safi-Harb in preparation; see also Matheson & Safi-Harb 2005). The individual components contributing to the fitted spectrum are shown as dashed lines. The bottom panel shows the data-to-model ratios and illustrates that this model does not reproduce the spectral shape obtained with the HXI. (Color online)

with the Hitomi data. This conclusion was similarly reached by the NuSTAR study (Nynka et al. 2014).

To that end, we construct a composite power-law model consisting of spatially resolved spectra of 50 regions obtained with all Chandra data acquired to date (B. Guest & S. Safi-Harb in preparation; see also Matheson & Safi-Harb 2005). The model accounts for the small-scale regions extending from the pulsar out to the SNR limb and consists of power-law model components with an index steepening from ~ 1.5 at the pulsar to ~ 2.6 in the outermost region. Fitting this composite model to the Hitomi spectra clearly shows that the model does not fit the HXI data, as shown in figure 3.

We have to consider possible mechanisms to make the spectral break other than the spatial variation of the synchrotron radiation. Let us discuss this in the context of a multi-wavelength study using data from radio up to TeV gamma rays including the Hitomi data. Many authors have been trying to reproduce spectral energy distributions of PWNe such as the Crab nebula and G21.5–0.9 in the literature (e.g., Atoyan & Aharonian 1996; Zhang et al. 2008; Tanaka & Takahara 2010, 2011; Martín et al. 2012; Torres et al. 2014). In what follows, we calculate emission models for G21.5–0.5 based on the one-zone model by Tanaka and Takahara (2010, 2011).

The PWN is assumed to be a uniform sphere with a radius of R_{pwn} expanding with a constant velocity v_{pwn} (i.e., $R_{\text{pwn}} = v_{\text{pwn}}t$). The spin-down power of the central pulsar

is expressed as

$$L_{\text{sd}}(t) = L_{\text{sd}0} \left(1 + \frac{t}{\tau_0} \right)^{-\frac{n+1}{n-1}}, \quad (1)$$

where $L_{\text{sd}0}$, τ_0 , and n are the initial spin-down luminosity, the initial spin-down timescale, and the breaking index, respectively. The spin-down luminosity is finally converted either to kinetic power of relativistic positrons and electrons (we refer to these simply as electrons hereafter) L_e or into magnetic power L_B in the PWN region. The ratio of the two channels is determined by the temporally and spatially constant parameter η ($0 \leq \eta \leq 1$) as

$$L_e(t) = (1 - \eta)L_{\text{sd}}(t), \quad (2)$$

$$L_B(t) = \eta L_{\text{sd}}(t). \quad (3)$$

Electrons are injected into the PWN with a broken power-law spectrum:

$$Q(E, t) = \begin{cases} Q_0(t)(E/E_b)^{-p_1} & (E_{\min} \leq E < E_b) \\ Q_0(t)(E/E_b)^{-p_2} & (E_b \leq E \leq E_{\max}) \\ 0 & (\text{otherwise}), \end{cases} \quad (4)$$

where E denotes the kinetic energy of the electrons and E_b is the break energy. The normalization $Q_0(t)$ can be obtained by substituting

$$L_e(t) = \int_{E_{\min}}^{E_{\max}} E Q(E, t) dE \quad (5)$$

into equation (2). The magnetic energy conservation,

$$\frac{4\pi}{3} [R_{\text{PWN}}(t)]^3 \frac{[B(t)]^2}{8\pi} = \int_0^t \eta L(t') dt', \quad (6)$$

together with equation (1) yields the magnetic field strength

$$B(t) = \sqrt{\frac{3(n-1)\eta L_{\text{sd}0} \tau_0}{[R_{\text{PWN}}(t)]^3} \left[1 - \left(1 + \frac{t}{\tau_0} \right)^{-\frac{2}{n-1}} \right]}. \quad (7)$$

The electron spectrum at time t is obtained by solving the Fokker–Planck equation

$$\frac{\partial N(E, t)}{\partial t} = \frac{\partial}{\partial E} [b(E, t) N(E, t)] + Q(E, t) \quad (8)$$

for $N(E, t)$, where $b(E, t)$ is the energy loss rate of electrons. We consider energy losses by synchrotron, IC, and adiabatic expansion of the PWN. We then calculate synchrotron and IC radiation spectra from the electrons with the spectrum $N(E, t_{\text{age}})$, where t_{age} is the age of the pulsar. In the calculation of the synchrotron spectrum, we assume

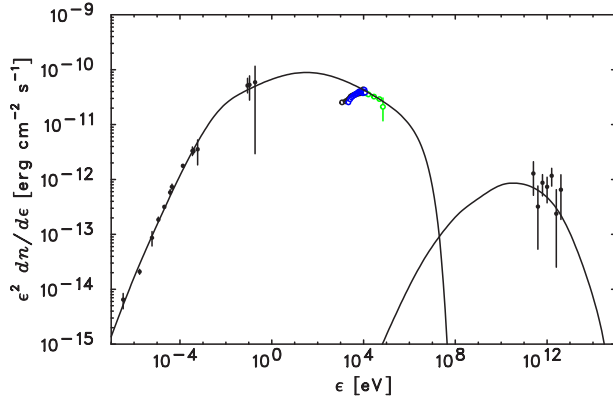


Fig. 4. Spectral energy distribution of G21.5–0.9 with the Case 1 model whose parameters are summarized in table 3. The black, blue, and green data points in the X-ray band are from the SXI, SXS, and HXI, respectively. The data from HXI1 and HXI2 are co-added for display purposes. The radio data points are taken from Wilson and Weiler (1976), Becker and Kundu (1975), Morsi and Reich (1987), and Salter et al. (1989). The infrared data were obtained with the Infrared Space Observatory by Gallant and Tufts (1999). The H.E.S.S. data points in the TeV gamma-ray band are by Djannati-Ataï et al. (2008). (Color online)

that the magnetic field line directions are randomly distributed, and use the analytical formula for the synchrotron spectrum from a single electron by Zirakashvili and Aharonian (2007). We consider isotropic radiation fields for IC, and calculate the spectrum by using the expression given by Jones (1968). The radiation fields' spectra are taken from the model implemented in GALPROP (Porter et al. 2006), which includes the cosmic microwave background, optical radiation from stars, and infrared radiation due to reemission of the optical component by dust.

We first tried fitting the overall shape of the multi-wavelength spectrum of G21.5–0.9 (Case 1). Figure 4 shows the result of the calculation plotted with the data in the radio, infrared, X-ray, and TeV gamma-ray bands. In the calculation, we assumed 4.7 kpc as the distance to the PWN (Camilo et al. 2006). Referring to Bietenholz and Bartel (2008), we assumed the expansion velocity of the PWN and the age of the pulsar to be $v_{\text{pwn}} = 910 \text{ km s}^{-1}$ and $t_{\text{age}} = 870 \text{ yr}$, respectively. Since the second derivative of the pulsar period has not been measured, we simply assumed $n = 3$, which corresponds to spin-down via magnetic dipole radiation. The rotation period P and period derivative \dot{P} of PSR J1833–1034 are taken from Camilo et al. (2006) as $P = 61.9 \text{ ms}$ and $\dot{P} = 2.02 \times 10^{-13}$, which are used to obtain τ_0 and $L_{\text{sd0}} \tau_0$ as

$$\tau_0 = \frac{P}{(n-1)\dot{P}} - t_{\text{age}} = 4.0 \text{ kyr}, \quad (9)$$

$$P_0 = P \left(1 + \frac{t_{\text{age}}}{\tau_0} \right)^{-\frac{1}{n-1}} = 56 \text{ ms}, \quad (10)$$

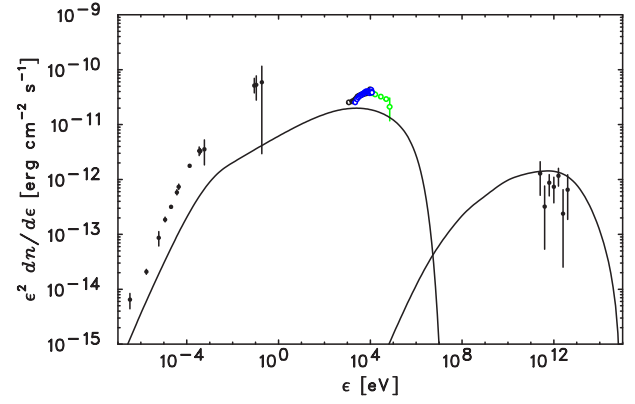


Fig. 5. As figure 4, but with the Case 2 model curves. (Color online)

Table 3. Parameters for model calculations.

	η	E_{min}	E_{b}	E_{max}	p_1	p_2
Case 1	2.0×10^{-2}	0.5 GeV	50 GeV	1 PeV	1.0	2.5
Case 2	1.0×10^{-3}	0.5 GeV	50 GeV	1 PeV	1.0	2.5

$$L_{\text{sd0}} \tau_0 = \frac{I}{(n-1)\tau_0} \left(\frac{2\pi}{P_0} \right)^2 = 6.3 \times 10^{48} \text{ erg}. \quad (11)$$

Here, P_0 is the initial pulsar period, and I is pulsar's moment of inertia for which we assumed 10^{45} g cm^2 . The parameters are similar to those of Model 1 by Tanaka and Takahara (2011). Although the model fits well the radio, infrared, and gamma-ray data points, it fails to fit the Hitomi spectra, particularly in the soft X-ray band below the break at 7 keV.

One of the possible mechanisms to make the X-ray spectral break is synchrotron cooling. In the model presented in figure 4, the synchrotron cooling break appears at $\sim 10^2 \text{ eV}$. Since the synchrotron cooling break energy is roughly proportional to B^{-3} , we need to have a weaker magnetic field and thus smaller η to move the break toward a higher energy up to the 7 keV at which we found the break. In figure 5, we plot model curves for which we assumed smaller η so that the synchrotron break coincides with the observed break (Case 2). The parameters are summarized in table 3. Smaller η results in a lower synchrotron-to-IC flux ratio, which contradicts the data. In addition, the model predicts a smaller spectral slope change at the break than the Hitomi data. The assumption about the magnetic field evolution in principle can affect the results. Several authors (e.g., Zhang et al. 2008; Torres et al. 2014) indeed considered different magnetic field evolution models. The situation, however, would not be drastically improved even if we adopt their assumptions.

Instead of synchrotron cooling, another break in the electron injection spectrum might be able to explain the break

we observed. This scenario, however, would not be feasible, at least with a one-zone model. As demonstrated by the Case 1 model shown in figure 4, the parameter η should be $\sim 10^{-2}$ to account for the observed synchrotron-to-IC ratio. In this case, the synchrotron cooling break inevitably appears at an energy below the X-ray band, which leads to a softer X-ray spectrum. It is then difficult to reproduce the low-energy part of the Hitomi spectrum, i.e., the hard spectrum below the break with a photon index of $\Gamma_1 = 1.7$.

It is likely that more complicated models are required to reproduce the observational data. We assumed a single electron population in an emitting region where physical parameters such as the magnetic field strength are uniform. In reality, electrons are transported from the termination shock of the PWN through advection and diffusion (de Jager et al. 2008; Tang & Chevalier 2012; Vorster & Moraal 2013). Higher-energy electrons suffer from significant synchrotron cooling, which makes the electron spectrum spatially variable. The magnetic field should have spatial variation as well. X-rays would be emitted by electrons close to the termination shock where the magnetic field is relatively high, while the radio-to-infrared radiation might be coming from a larger region. In this context, it is of interest to note that the radio and X-ray images presented by Matheson and Safi-Harb (2005) suggest different morphologies. The X-ray emission appears more concentrated close to the pulsar compared with the radio image. It is also possible that radio-emitting and X-ray-emitting electrons have different origins. Tanaka and Asano (2017) proposed such a model (see also Ishizaki et al. 2017). In their model, electrons responsible for X-rays are provided by the pulsar wind and are accelerated at the termination shock through the diffusive shock acceleration process. On the other hand, radio-emitting electrons are supplied, for example, by supernova ejecta, and are stochastically accelerated by turbulence inside a PWN. Such models could reproduce the complex synchrotron shape that the Hitomi result revealed.

4 Search for lines

4.1 Analysis

We performed a blind search for emission and absorption lines from the SXS spectrum. We focus on narrow lines in the 2–10 keV band. The bandpass is limited by the attenuation by the closed gate-valve below 2 keV and the photon statistics above 10 keV. Features with a width up to 1280 km s^{-1} were searched. A search for weak broad features is strongly coupled with the exact shape of the continuum, details of which are hampered by the incomplete calibration of the effective area of the SXS (Tsujiimoto et al. 2018).

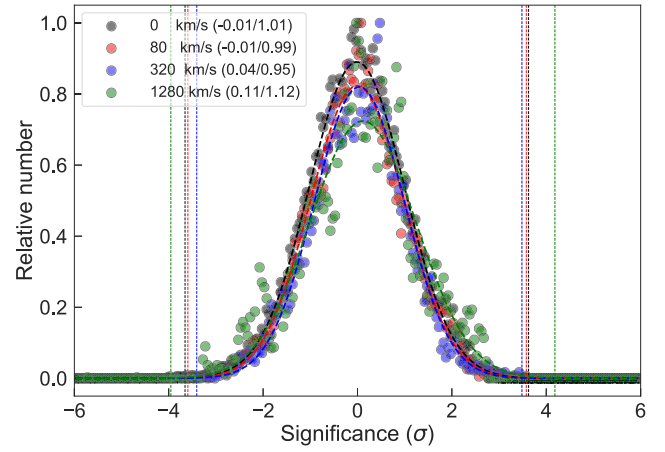


Fig. 6. Distribution of significance [equation (12)] for several selected trial widths in different colors. The distribution is fitted by a single Gaussian model, and its best-fit parameter is shown in the legend as (center, width). The horizontal dotted lines indicate the significance at which the upper or lower probability is 0.1% assuming the best-fit Gaussian distribution. (Color online)

We took the same approach as for the Crab nebula (Hitomi Collaboration 2018a), in which we fitted the spectrum locally and added a single Gaussian model with a fixed trial energy and width. The trial energies are from 2 to 10 keV with a 0.5 eV step, and the widths are 0, 20, 40, 80, 160, 320, 640, and 1280 km s^{-1} . The power-law model was used for the local continuum fitting in an energy range $3-20\sigma(E)$ on both sides of the trial energy E , in which $\sigma(E)$ is the quadrature sum of the trial width and the line spread function width. The significance of the detection was assessed as

$$\sigma = \frac{N_{\text{line}}}{\sqrt{\Delta N_{\text{line}}^2 + (N_{\text{line}} \Delta I_{\text{cont}} / I_{\text{cont}})^2}}, \quad (12)$$

in which N_{line} and ΔN_{line} are the best-fit and 1σ statistical uncertainty of the line normalization in units of $\text{s}^{-1} \text{ cm}^{-2}$, whereas I_{line} and ΔI_{line} are those of the continuum intensity in units of $\text{s}^{-1} \text{ cm}^{-2} \text{ keV}^{-1}$ at the line energy. Positive values indicate emission, whereas negative values indicate absorption.

Figure 6 shows the distribution of significance for some selected trial widths. The distribution of significances is well fitted by a simple Gaussian distribution. Assuming that it is indeed a single Gaussian distribution, we set the detection limit such that, on both sides, there is less than 0.01 false positives for the number of trials. There are nine trial absorption lines that lie in the tail of the distribution with the significance of the width deviations of 3.65σ . All of these lines are either at 4.2345 keV or 9.296 keV. We show the fits to the two most significant ones in figure 7. These modeled absorption lines yield an equivalent width of $-2.3 \pm 0.8 \text{ eV}$ and velocity widths of $50-400 \text{ km s}^{-1}$.

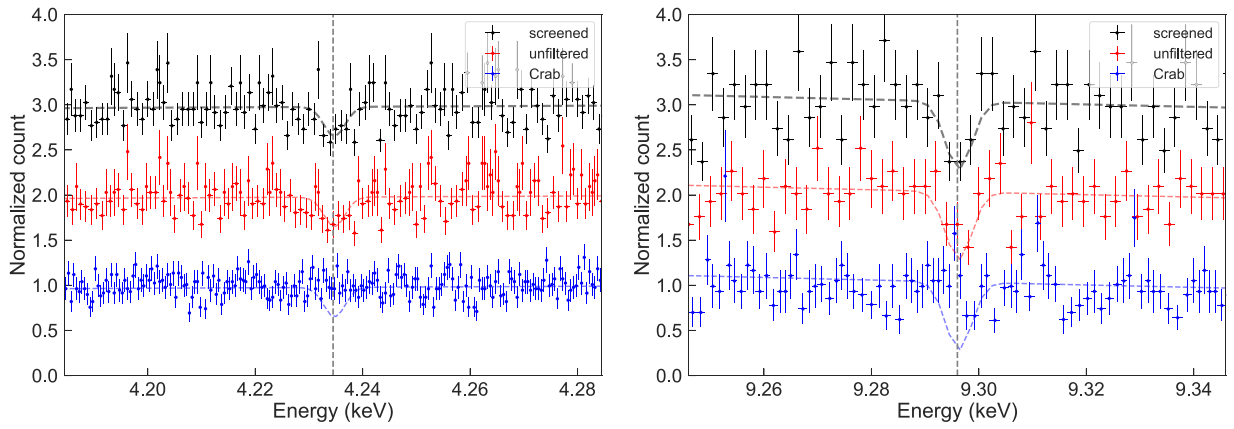


Fig. 7. Background-unsubtracted spectra at two energies (4.2345 keV and 9.296 keV for the left and right panels, respectively). Black, red, and blue respectively show the background-unsubtracted spectrum for the screened G21.5–0.9, the unfiltered G21.5–0.9, and the screened Crab data, which are normalized and offset to have a mean at 3.0, 2.0, and 1.0. The black dotted curve is the best-fit continuum plus Gaussian model for a velocity width of 0 km s^{−1}. The red and blue curves are the same model with a different offset to match the comparison data. (Color online)

Table 4. Parameters for detected absorption lines.

Line centroid (keV)	Equivalent width (eV)	Velocity width (km s ^{−1})	Significance (σ)
4.2345	-2.3 ± 0.8	50–400	3.65
9.296	-4.9 ± 2.2	<89	3.65

for 4.2345 keV and -4.9 ± 2.2 eV and <89 km s^{−1} for 9.296 keV. The results are summarized in table 4.

In figure 7, for comparison, we also plot the G21.5–0.9 spectrum made with unfiltered events and the Crab spectrum with screened events. The former is intended to examine artifacts by event screening, while the latter by the effective area calibration. For both energies, the absorption features are not seen in the Crab data (and other Hitomi datasets), indicating that they are not instrumental features. The features are seen both in the unfiltered and screened spectra, suggesting that they are not due to the screening.

4.2 Possible absorption line features

The method described above using the SXS data revealed absorption features around 4.2345 keV and 9.296 keV. Given that these lines are not present in other Hitomi data, including the Crab (an object similar in nature to G21.5–0.9), we propose an astrophysical origin. However, we cannot identify these lines as there are no known strong atomic transitions in nearby energies even if we consider the doppler effect due to the expansion.

One interpretation is electron cyclotron resonance scattering. The absorption feature would then be at

$$E_c = 11.6 \left(\frac{B}{10^{12} \text{ G}} \right) \text{ keV} \sim 42 \left(\frac{B}{3.6 \times 10^{12} \text{ G}} \right) \text{ keV} \quad (13)$$

for a surface dipole magnetic field strength of the pulsar of $B = 3.6 \times 10^{12}$ G, which is estimated from P and \dot{P} . If interpreted as electron cyclotron features, the absorption features would be associated with lower magnetic fields of the order of 4×10^{11} G and 8×10^{11} G for the 4.2345 keV and 9.296 keV lines, respectively. In this case, the absorbing electrons would be located higher in the magnetosphere. However, the line features are not as broad as we expect for cyclotron absorption lines, and the ratio of their energies (given the precise values determined by the SXS) is not 1 : 2, as would be expected from harmonics. We therefore rule out the possibility of the electron cyclotron absorption lines.

Another potential origin is surface atomic lines from the strongly magnetized neutron star atmosphere, as predicted by calculations with a high-field multiconfigurational Hartree–Fock code (Miller & Neuhauser 1991; Miller 1992, and references therein). While absorption features (or emission lines in a few cases) have been reported from a range of isolated neutron stars, from the extremely high magnetic field objects like magnetars (e.g., Turolla et al. 2015), to the extremely low magnetic field objects like the Central Compact Objects (e.g., Bignami et al. 2003), to the X-ray Dim Isolated Neutron Stars (Borghese et al. 2017), to even an isolated “ordinary” rotation-powered pulsar (Kargaltsev et al. 2012), these lines are all either relatively broad, or if similarly narrow (e.g., as seen in

XMM-Newton grating spectra of isolated neutron stars, Hohle et al. 2012), they are at much lower energies. Furthermore, the presence of the lines is controversial in some of these sources. The SXS features reported here in G21.5–0.9 are the first such narrow lines found in the hard X-ray band and for a rotation-powered pulsar powering a PWN.

More recently, Rajagopal, Romani, and Miller (1997) and Mori and Ho (2007) constructed models of magnetized atmospheres composed of Fe and mid-Z elements, respectively. According to their calculations and simulated spectra, multiple absorption features appear in the energy range from ~ 0.1 keV up to ~ 10 keV. We note that if the atmosphere is dominated by O or Ne (Mori & Ho 2007), a magnetic field strength of $B > 10^{13}$ G is required to explain the observed line feature at an energy as high as 9.296 keV. Given the magnetic field of PSR J1833–1034, $B = 3.6 \times 10^{12}$ G, we speculate that heavier elements may be dominant in its atmosphere (unless we are probing higher-order strong multipoles). This then suggests fallback of supernova ejecta onto the neutron star surface. While the pulsar powering G21.5–0.9 is believed to be an isolated pulsar, the possibility of fallback would be interesting in the light of PSR J1833–1034 being likely the youngest known pulsar in our Galaxy with a PWN age estimated at only 870 yr (Bietenholz & Bartel 2008). It is, however, difficult to identify a specific element only from the two faint features. The Thomson depth has a complicated structure and the resultant spectra show many absorption lines whose centroids highly depend on B and the temperature of the atmosphere (Mori & Ho 2007).

Lastly, another potential origin is absorption associated with its surroundings, noting that the PWN has a significant dust scattering halo. Again, however, the line energies are much too high to be associated with an ISM component. The lack of detection of X-ray pulsations (section 5) hampers a phase-resolved spectroscopic study which would help differentiate between an intrinsic-to-the-pulsar or ambient origin. Future deep observations of PSR J1833–1034 with a high-resolution spectrometer, as well as the detection of similarly narrow hard X-ray absorption features from other similar systems, will help reveal the nature of these features, and may open a new window for studying the atmospheres or environment of isolated pulsars.

5 Search for coherent pulsation

We searched the HXI and SGD data for pulsed signals from the central pulsar PSR J1833–1034. Before analyzing the data, we estimated the expected period of the pulsar during the Hitomi observation. The measured P in radio and GeV observations (Gupta et al. 2005; Camilo et al. 2006; Abdo et al. 2013) show a straight linear increase

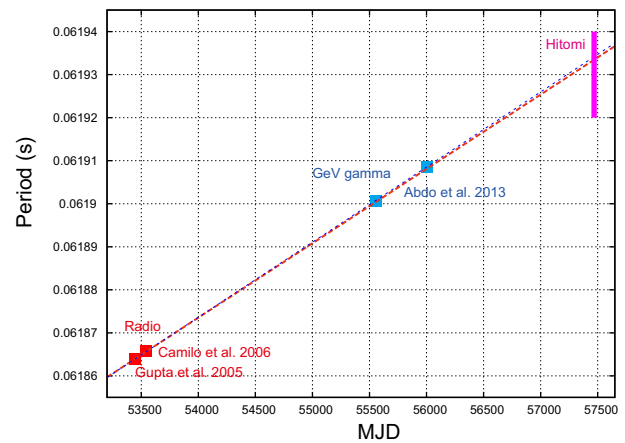


Fig. 8. Period measurements of PSR J1833–1034 in the radio and GeV gamma-ray band (Gupta et al. 2005; Camilo et al. 2006; Abdo et al. 2013), shown in red and cyan, respectively. The search area with Hitomi is shown in magenta. (Color online)

with time, as shown in figure 8. The slope is consistent with $\dot{P} = 2.2025(3) \times 10^{-13} \text{ s s}^{-1}$, the result of the most detailed observation (Camilo et al. 2006). We thus decided to search for P in the range 61.92–61.94 ms, and fixed $\dot{P} = 2.2025 \times 10^{-13} \text{ s s}^{-1}$.

Extracting the HXI events, we tried two sizes of circular regions with $8''$ and $70''$ radii centered at (RA, Dec) = $(18^{\text{h}}33^{\text{m}}33^{\text{s}}.8, -10^{\circ}34'01'')$ for better signal-to-noise ratio for the pulsar against the PWN and the pulsar against the background, respectively. In the extraction of the SGD events, the photo-absorption events were extracted following the method described in the appendix 2 of Hitomi Collaboration (2018b). We applied the barycentric correction on the arrival times of events using *barycen* for Hitomi (Terada et al. 2017). The timing searches were performed in each of the following energy bands: 20–30 keV, 30–40 keV, 40–50 keV, 50–60 keV, and 60–70 keV for the HXI, and 20–30 keV, 30–50 keV, 50–100 keV, and 100–200 keV for the SGD. As a result, about 10–170 events were obtained per energy band for the HXI smaller region, about 370–2800 events for the HXI larger region, and about 12000–17000 events for the SGD. We performed *efserach* in HEASoft 6.20 with a time resolution of 1 ns on four sets of phase bin sizes (5, 7, 13, and 23 bins) with five different time origins (shifted by 0, 20%, 40%, 60%, and 80% of each phase-bin size) and found no significant pulsation (i.e., the values of $\chi^2/\text{d.o.f.}$ of trial-pulse profiles to the constant model are close to unity for all the trials). We estimated the 5σ values of the $\chi^2/\text{d.o.f.}$ on all the trials, as summarized in table 5. In comparison of these χ^2 values with the numerical simulations of possible pulses under the assumption that the pulse profiles have sinusoidal shapes in various amplitudes, the pulse fractions corresponding to the 5σ values of the $\chi^2/\text{d.o.f.}$ were also estimated (table 5);

Table 5. Timing search results for each setting.

Instrument	Region	Energy band (keV)	Count*	$\chi^2/\text{d.o.f.}^\dagger$	Pulse fraction [‡] (%)	count s ^{-1‡}
HXI	8'' circle	30–40	168	4.5,3.8,3.0,2.5	24,26,30,35	$<2.4 \times 10^{-4}$
HXI	8'' circle	40–50	90	4.5,3.9,3.0,2.5	31,34,39,41	$<1.6 \times 10^{-4}$
HXI	8'' circle	50–60	28	4.7,4.0,3.1,2.5	41,42,41,41	$<5.8 \times 10^{-5}$
HXI	8'' circle	60–70	10	4.4,3.8,3.0,2.5	42,42,42,42	$<2.1 \times 10^{-5}$
HXI	70'' circle	30–40	2768	4.7,4.0,3.1,2.5	6, 7, 9,10	$<1.1 \times 10^{-3}$
HXI	70'' circle	40–50	1218	4.5,3.9,3.0,2.5	10,11,13,14	$<7.3 \times 10^{-4}$
HXI	70'' circle	50–60	628	4.6,3.9,3.1,2.5	13,15,18,20	$<5.2 \times 10^{-4}$
HXI	70'' circle	60–70	370	4.6,3.9,3.1,2.5	17,19,22,25	$<3.9 \times 10^{-4}$
SGD	–	20–30	11766	4.5,3.9,3.0,2.5	3, 3, 4, 5	$<1.7 \times 10^{-3}$
SGD	–	30–50	12401	4.7,3.9,3.1,2.5	3, 3, 4, 5	$<1.8 \times 10^{-3}$
SGD	–	50–100	17069	4.5,3.9,3.0,2.5	2, 3, 3, 4	$<2.0 \times 10^{-3}$
SGD	–	100–200	14855	4.4,3.8,3.0,2.5	2, 3, 3, 4	$<1.7 \times 10^{-3}$

* Total number of events, including background.

[†] 5σ upper limit by searches in the 5, 7, 13, and 23 phase bins, respectively.

[‡] 5σ upper limit in count rate.

the pulse fractions become similar values among various phase-bin settings, although $\chi^2/\text{d.o.f.}$ varies by the settings. The 5σ upper limits in the count rate in each energy band were also estimated in the table. We also tried Z^m analysis (Buccheri et al. 1983; Brazier 1994) for the same data set, in order to reduce high-frequency noise. Again, no significant pulsation was found.

6 Summary

While a standard pulsar wind theory of the Crab Nebula has been established by Kennel and Coroniti (1984), there are many evolution models proposed to generally describe the spectra of PWNe from radio to gamma rays. G21.5–0.9 is a good example to investigate the emission mechanism in this context since the remnant is considered to be a prototype pulsar/PWN system in the early stage of evolution (cf. Gaensler & Slane 2006). We observed G21.5–0.9 with Hitomi on 2016 March 19–23 during the instrument commissioning and verification phase of the satellite. Thanks to their high sensitivity, wide-band spectra obtained with the SXS, SXI, and HXI on-board Hitomi revealed a detailed spectral feature in the range of 0.8–80 keV where a spectral break had been pointed out by previous studies (Tsujimoto et al. 2011; Nynka et al. 2014). We constructed a “composite” spectral model accounting for all components of G21.5–0.9 to constrain the break energy of the central PWN. Our results indicate that the PWN spectrum is reproduced by a broken power-law model with photon indices of $\Gamma_1 = 1.74 \pm 0.02$ and $\Gamma_2 = 2.14 \pm 0.01$ below and above the break, respectively. The break energy E_{break} is located at 7.1 ± 0.3 keV, which is significantly lower than that estimated from the NuSTAR spectra ($9.0^{+0.6}_{-0.4}$ keV in the 30inner region) by Nynka et al. (2014). We attempted

to explain the SED from radio to TeV gamma rays with a spectral evolution model based on the work by Tanaka and Takahara (2010, 2011). The overall shape of the multi-wavelength spectrum is well fitted by the model, whereas it fails to reproduce the Hitomi spectra particularly in the soft X-ray band below the break. Our results require more complicated models considering, for example, stochastic acceleration (e.g., Tanaka & Asano 2017). We also performed a timing analysis and a thermal line search of G21.5–0.9 with the Hitomi instruments: no significant pulsation was found from PSR J1833–1034 with the HXI and SGD. Two narrow absorption line features were detected at 3.65σ confidence at 4.2345 keV and 9.296 keV in the SXS spectrum. The observed absorption features reported here are not seen in the Crab data or other Hitomi datasets, suggesting that they are not an instrumental artifact. The nature of these features is not well understood, but their mere detection opens up a new area of research in the physics of plerions and isolated pulsars, and is a challenge to present-day models. It is highly surprising in that the spectrum of what was supposed to be a featureless calibration source shows significant unexpected spectral features. This indicates the power of the X-ray microcalorimeter for opening up a new discovery space in astrophysics.

Author contributions

H. Uchida, T. Tanaka, and S. Safi-Harb led the data analysis and draft preparation. The wide-band spectroscopy was performed mainly by H. Uchida, T. Tanaka, S. Safi-Harb, Y. Maeda, N. Nakaniwa, and B. Guest. The thermal line search was done by M. Tsujimoto and T. Sato. Y. Terada took responsibility for the timing analysis with the help

of H. Murakami. A. Bamba coordinated the analysis tasks for each topic. The paper was improved by J. P. Hughes, R. Mushotzky, and M. Sawada.

Acknowledgments

We thank D. A. Smith and M. Kerr for giving us the detailed information on the Fermi LAT observations of PSR J1833–1034. We acknowledge the support from the JSPS Core-to-Core Program, and all the JAXA members who have contributed to the ASTRO-H (Hitomi) project. All U.S. members gratefully acknowledge support through the NASA Science Mission Directorate. Stanford and SLAC members acknowledge support via the DoE contract to the SLAC National Accelerator Laboratory DE-AC3-76SF00515. Part of this work was performed under the auspices of the U.S. DoE by LLNL under Contract DE-AC52-07NA27344. Support from the European Space Agency is gratefully acknowledged. French members acknowledge support from CNES, the Centre National d'Études Spatiales. SRON is supported by NWO, the Netherlands Organization for Scientific Research. The Swiss team acknowledges the support of the Swiss Secretariat for Education, Research and Innovation (SERI). The Canadian Space Agency is acknowledged for the support of the Canadian members. We acknowledge support from JSPS/MEXT KAKENHI grant numbers JP15H00773, JP15H00785, JP15H02070, JP15H02090, JP15H03639, JP15H03641, JP15H03642, JP15H05438, JP15H06896, JP15K05107, JP15K17610, JP15K17657, JP16H00949, JP16H03983, JP16H06342, JP16J02333, JP16K05295, JP16K05296, JP16K05300, JP16K05309, JP16K13787, JP16K17667, JP16K17672, JP16K17673, JP17H02864, JP17K05393, JP21659292, JP23340055, JP23340071, JP23540280, JP24105007, JP24540232, JP25105516, JP25109004, JP25247028, JP25287042, JP25400236, JP25800119, JP26109506, JP26220703, JP26400228, JP26610047, and JP26800102. The following NASA grants are acknowledged: NNX15AC76G, NNX15AE16G, NNX15AK71G, NNX15AU54G, NNX15AW94G, and NNG15PP48P to Eureka Scientific. This work was partly supported by Leading Initiative for Excellent Young Researchers, MEXT, Japan, and also by the Research Fellowship of JSPS for Young Scientists. H. Akamatsu acknowledges the support of NWO via a Veni grant. C. Done acknowledges STFC funding under grant ST/L00075X/1. A. Fabian and C. Pinto acknowledge ERC Advanced Grant 340442. P. Gandhi acknowledges JAXA International Top Young Fellowship and UK Science and Technology Funding Council (STFC) grant ST/J003697/2. Y. Ichinohe and K. Nobukawa are supported by the Research Fellow of JSPS for Young Scientists. N. Kawai is supported by the Grant-in-Aid for Scientific Research on Innovative Areas “New Developments in Astrophysics Through Multi-Messenger Observations of Gravitational Wave Sources.” S. Kitamoto is partially supported by the MEXT Supported Program for the Strategic Research Foundation at Private Universities, 2014–2018. B. McNamara and S. Safi-Harb acknowledge support from NSERC. T. Dotani, T. Takahashi, T. Tamagawa, M. Tsujimoto, and Y. Uchiyama acknowledge support from the Grant-in-Aid for Scientific Research on Innovative Areas “Nuclear Matter in Neutron Stars Investigated by Experiments and Astronomical Observations.” N. Werner is supported by the Lendület LP2016-11 grant from the Hungarian Academy of Sciences. D. Wilkins is supported by NASA through Einstein Fellowship grant number PF6-170160, awarded by the Chandra X-ray Center, operated

by the Smithsonian Astrophysical Observatory for NASA under contract NAS8-03060. We are grateful for contributions by many companies, including in particular, NEC, Mitsubishi Heavy Industries, Sumitomo Heavy Industries, and Japan Aviation Electronics Industry.

Finally, we acknowledge strong support from the following engineers. JAXA/ISAS: Chris Baluta, Nobutaka Bando, Atsushi Harayama, Kazuyuki Hirose, Kosei Ishimura, Naoko Iwata, Taro Kawano, Shigeo Kawasaki, Kenji Minesugi, Chikara Natsukari, Hiroyuki Ogawa, Mina Ogawa, Masayuki Ohta, Tsuyoshi Okazaki, Shin-ichiro Sakai, Yasuko Shibano, Maki Shida, Takanobu Shimada, Atsushi Wada, Takahiro Yamada; JAXA/TKSC: Atsushi Okamoto, Yoichi Sato, Keisuke Shinozaki, Hiroyuki Sugita; Chubu U: Yoshiharu Namba; Ehime U: Keiji Ogi; Kochi U of Technology: Tatsuro Kosaka; Miyazaki U: Yusuke Nishioka; Nagoya U: Housei Nagano; NASA/GSFC: Thomas Bialas, Kevin Boyce, Edgar Canavan, Michael DiPirro, Mark Kimball, Candace Masters, Daniel McGuinness, Joseph Miko, Theodore Muench, James Pontius, Peter Shirron, Cynthia Simmons, Gary Sneiderman, Tomomi Watanabe; ADNET Systems: Michael Witthoef, Kristin Rutkowski, Robert S. Hill, Joseph Eggen; Wyle Information Systems: Andrew Sargent, Michael Dutka; Noqi Aerospace Ltd: John Doty; Stanford U/KIPAC: Makoto Asai, Kirk Gilmore; ESA (Netherlands): Chris Jewell; SRON: Daniel Haas, Martin Frericks, Philippe Laubert, Paul Lowes; U of Geneva: Philipp Azzarello; CSA: Alex Koujelev, Franco Moroso.

References

- Abdo, A. A., et al. 2013, *ApJS*, 208, 17
- Altenhoff, W. J., Downes, D., Goad, L., Maxwell, A., & Rinehart, R. 1970, *A&AS*, 1, 319
- Anders, E., & Grevesse, N. 1989, *Geochim. Cosmochim. Acta*, 53, 197
- Arnaud, K. A. 1996, in *ASP Conf. Ser.*, 101, *Astronomical Data Analysis Software and Systems V*, ed. G. H. Jacoby & J. Barnes (San Francisco: ASP), 17
- Atoyan, A. M., & Aharonian, F. A. 1996, *MNRAS*, 278, 525
- Awaki, H., et al. 2014, *Appl. Opt.*, 53, 7664
- Bamba, A., Mori, K., & Shibata, S. 2010, *ApJ*, 709, 507
- Becker, R. H., & Kundu, M. R. 1975, *AJ*, 80, 679
- Becker, R. H., & Szymkowiak, A. E. 1981, *ApJL*, 248, L23
- Bietenholz, M. F., & Bartel, N. 2008, *MNRAS*, 386, 1411
- Bignami, G. F., Caraveo, P. A., De Luca, A., & Mereghetti, S. 2003, *Nature*, 423, 725
- Bocchino, F., van der Swaluw, E., Chevalier, R., & Bandiera, R. 2005, *A&A*, 442, 539
- Borghese, A., Rea, N., Coti Zelati, F., Tiengo, A., Turolla, R., & Zane, S. 2017, *MNRAS*, 468, 2975
- Borkowski, K. J., Lyerly, W. J., & Reynolds, S. P. 2001, *ApJ*, 548, 820
- Brazier, K. T. S. 1994, *MNRAS*, 268, 709
- Buccheri, R., et al. 1983, *A&A*, 128, 245
- Camilo, F., Ransom, S. M., Gaensler, B. M., Slane, P. O., Lorimer, D. R., Reynolds, J., Manchester, R. N., & Murray, S. S. 2006, *ApJ*, 637, 456
- Cash, W. 1979, *ApJ*, 228, 939
- de Jager, O. C., Ferreira, S. E. S., & Djannati-Ataï, A. 2008, in *AIP Conf. Proc.*, 1085, *High Energy Gamma-Ray Astronomy: Proc.*

- 4th Int. Meeting on High Energy Gamma-Ray Astronomy, ed. F. A. Aharonian et al. (New York: AIP), 199
- Djannati-Ataï, A., deJager, O. C., Terrier, R., Gallant, Y. A., & Hoppe, S. 2008, *Int. Cosmic Ray Conf.*, 2, 823
- Fang, J., & Zhang, L. 2010, *A&A*, 515, A20
- Gaensler, B. M., & Slane, P. O. 2006, *ARA&A*, 44, 17
- Gallant, Y. A., & Tuffs, R. J. 1999, in *The Universe as Seen by ISO*, ed. P. Cox & M. F. Kessler, ESA SP-427 (Noordwijk: ESA), 313
- Gupta, Y., Mitra, D., Green, D. A., & Acharyya, A. 2005, *Current Sci.*, 89, 853
- Hagino, K., et al. 2018, *J. Astron. Telesc. Instrum. Syst.*, in press
- Hitomi Collaboration 2018a, *PASJ*, 70, 14
- Hitomi Collaboration 2018b, *PASJ*, 70, 15
- Hohle, M. M., Haberl, F., Vink, J., de Vries, C. P., & Neuhauser, R. 2012, *MNRAS*, 419, 1525
- Hughes, J. P., Rakowski, C. E., Burrows, D. N., & Slane, P. O. 2000, *ApJ*, 528, L109
- Ishizaki, W., Tanaka, S. J., Asano, K., & Terasawa, T. 2017, *ApJ*, 838, 142
- Jones, F. C. 1968, *Phys. Rev.*, 167, 1159
- Kargaltsev, O., Durant, M., Misanovic, Z., & Pavlov, G. G. 2012, *Science*, 337, 946
- Kargaltsev, O., & Pavlov, G. G. 2008, in *AIP Conf. Proc.*, 983, 40
- Years of Pulsars: Millisecond Pulsars, Magnetars and More, ed. C. Bassa et al. (New York: AIP), 171
- Kelley, R. L., et al. 2016, *Proc. SPIE*, 9905, 99050V
- Kennel, C. F., & Coroniti, F. V. 1984, *ApJ*, 283, 694
- Kirsch, M. G., et al. 2005, *Proc. SPIE*, 5898, 22
- Martín, J., Torres, D. F., & Rea, N. 2012, *MNRAS*, 427, 415
- Matheson, H., & Safi-Harb, S. 2005, *Adv. Space Res.*, 35, 1099
- Matheson, H., & Safi-Harb, S. 2010, *ApJ*, 724, 572
- Matsumoto, H., et al. 2017, *J. Astron. Telesc. Instrum. Syst.* submitted
- Meszaros, P., & Nagel, W. 1985, *ApJ*, 298, 147
- Miller, M. C. 1992, *MNRAS*, 255, 129
- Miller, M. C., & Neuhauser, D. 1991, *MNRAS*, 253, 107
- Mori, K., & Ho, W. C. G. 2007, *MNRAS*, 377, 905
- Morsi, H. W., & Reich, W. 1987, *A&AS*, 69, 533
- Nakajima, H., et al. 2018, *PASJ*, 70, 21
- Nakazawa, K., et al. 2018, *J. Astron. Telesc. Instrum. Syst.*, in press
- Nynka, M., et al. 2014, *ApJ*, 789, 72
- Okajima, T., et al. 2016, *Proc. SPIE*, 9905, 99050Z
- Pacini, F., & Salvati, M. 1973, *ApJ*, 186, 249
- Porter, T. A., Moskalenko, I. V., & Strong, A. W. 2006, *ApJ*, 648, L29
- Rajagopal, M., Romani, R. W., & Miller, M. C. 1997, *ApJ*, 479, 347
- Rees, M. J., & Gunn, J. E. 1974, *MNRAS*, 167, 1
- Reynolds, S. P., & Chevalier, R. A. 1984, *ApJ*, 278, 630
- Reynolds, S. P., & Keohane, J. W. 1999, *ApJ*, 525, 368
- Safi-Harb, S., Harrus, I. M., Petre, R., Pavlov, G. G., Koptsevich, A. B., & Sanwal, D. 2001, *ApJ*, 561, 308
- Salter, C. J., Reynolds, S. P., Hogg, D. E., Payne, J. M., & Rhodes, P. J. 1989, *ApJ*, 338, 171
- Slane, P., Chen, Y., Schulz, N. S., Seward, F. D., Hughes, J. P., & Gaensler, B. M. 2000, *ApJ*, 533, L29
- Soong, Y., et al. 2014, *Proc. SPIE*, 9144, 914428
- Takahashi, T., et al. 2016, *Proc. SPIE*, 9905, 99050U
- Tanaka, S. J., & Asano, K. 2017, *ApJ*, 841, 78
- Tanaka, S. J., & Takahara, F. 2010, *ApJ*, 715, 1248
- Tanaka, S. J., & Takahara, F. 2011, *ApJ*, 741, 40
- Tanaka, T., et al. 2018, *J. Astron. Telesc. Instrum. Syst.*, 4, 011211
- Tang, X., & Chevalier, R. A. 2012, *ApJ*, 752, 83
- Terada, Y., et al. 2017, *J. Astron. Telesc. Instrum. Syst.*, 4, 011206
- Torres, D. F., Cillis, A., Martín, J., & de Oña Wilhelmi, E. 2014, *J. High Energy Astrophys.*, 1, 31
- Tsujimoto, M., et al. 2011, *A&A*, 525, A25
- Tsujimoto, M., et al. 2018, *PASJ*, 70, 20
- Turolla, R., Zane, S., & Watts, A. L. 2015, *Rep. Prog. Phys.*, 78, 116901
- Vorster, M. J., & Moraal, H. 2013, *ApJ*, 765, 30
- Warwick, R. S., et al. 2001, *A&A*, 365, L248
- Watanabe, S., et al. 2016, *Proc. SPIE*, 9905, 990513
- Wilms, J., Allen, A., & McCray, R. 2000, *ApJ*, 542, 914
- Wilson, A. S., & Weiler, K. W. 1976, *A&A*, 53, 89
- Yaqoob, T., et al. 2018, *J. Astron. Telesc. Instrum. Syst.* submitted
- Zhang, L., Chen, S. B., & Fang, J. 2008, *ApJ*, 676, 1210
- Zirakashvili, V. N., & Aharonian, F. 2007, *A&A*, 465, 695